Single NV centers as sensors for radio-frequency fields

Jingfu Zhang● and Dieter Suter●

Fakultät Physik, Technische Universität Dortmund, D-44221 Dortmund, Germany

We show that a single electron spin can serve as a sensor for radio-frequency (rf) magnetic fields. The longitudinal and transverse components of the rf field can be extracted from the phase acquired during free evolution of the spin coherence. In our experimental demonstration, a single electron spin of an NV center in diamond serves as an atomic size of two components of an rf field.

Introduction. Quantum sensing can be defined as the use of the quantum properties of a probing system (sensor) for measuring physical quantities, such as temperature, time, and electric and magnetic fields [1]. Quantum systems that can be used as sensors include ensembles of nuclear spins [2], atomic vapors [3,4], trapped ions [5,6], Rydberg atoms [7], superconducting circuits [e.g., superconducting quantum interference devices (SQUIDs)] [8–10], and nitrogen-vacancy (NV) centers in diamond, either in the form of ensembles or single spins [11–14].

Over the last years, it became evident that developments in different quantum technologies can generate useful synergies. As an example, progress in quantum sensing can be supported by algorithms and concepts developed for quantum information, where the quantum bits (qubits) are used for processing information [15,16]. The information content of a quantum state is the essential property for optimal performance and can be used to determine fundamental limits to the sensitivity of a specific sensing modality [17]. In both fields, the information must be protected against unwanted environmental noise [18], while the interactions with the environment can be tailored such that the sensor extracts the targeted information but rejects unwanted perturbations [19]. Techniques such as dynamical decoupling (DD) [20–24] or quantum error correction [18,25,26] and extended quantum memories [20,27–31] can enhance the sensitivity of quantum sensing.

Here, we focus on using single electron spins from NV centers in diamond [13] as quantum sensors for oscillating magnetic fields, i.e., ac fields. The main advantages of the NV centers for quantum sensing include high sensitivity, precision, and spatial resolution down to the atomic scale, e.g., measuring the local static (dc) magnetic fields produced by nuclear spins in diamond [32,33]. These beneficial properties are associated with the strong interaction between the electron spin and magnetic fields. Powerful control operations have been developed for this sensor, using resonant microwave fields and optical excitation. Readout is accomplished through efficient single-photon counting techniques. NV centers have been used as quantum sensors in biological systems, to provide access and insight into the structure and function of individual biomolecules and observe biological processes at the quantum level with atomic resolution [34].

NV centers can perform as sensors for both dc and ac magnetic fields, with one or multiple centers, e.g., based on Rabi oscillation or spin locking [1,11,35–42]. Most previous works on ac magnetometry were based on pulsed DD or continuous driving techniques such as spin locking [11,35]. However, with this approach, the frequency or the strength of the ac field that can be detected is limited by the Rabi frequency of the DD pulses, and the continuous microwave (MW) driving or too many DD pulses might cause undesired effects, such as MW broadening. Moreover, these techniques are only sensitive to dc fields or to ac fields in a very narrow frequency range, with known frequencies and phases because they require synchronization of the DD sequence with the ac field [23].

In this Letter, we propose and experimentally demonstrate a different strategy that does not suffer from these limitations: We encode the longitudinal and the transverse terms of an ac magnetic field in the phase of a coherent superposition of different spin states, where the MW fields are used only to generate and detect the coherence and therefore do not put any limitations to the fields to be measured, so that our strategy is applicable to broadband and unknown sources. Moreover, in contrast to existing approaches, our scheme can detect multiple frequency components simultaneously. The experiments were performed at room temperature, using a diamond sample isotopically enriched in ^{12}C to 99.995% [43–45].

Theory. The interaction between the electron spin and the ed field can be described by the Hamiltonian

$$\mathcal{H}_e(t) = (\omega_z S_z + \omega_x S_x)\sin(\omega_{\rm rf}t + \varphi_0). \tag{1}$$

Here, the amplitudes of the z and x component of the rf field are $\omega_z = -\gamma_e B^{\rm rf}_{1,z}$, $\omega_x = -\gamma_e B^{\rm rf}_{1,x}$, and φ_0 denotes the initial phase of the rf field. S_z and S_x denote the spin-1 operators for the electron. We use a coordinate system where the z axis is oriented along the symmetry axis of the NV and the rf field lies in the xz plane. The first term in Eq. (1) describes the
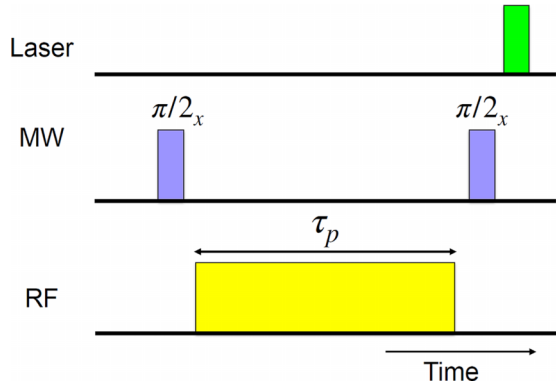
FIG. 1. Pulse sequence for sensing rf fields using the electron spin, which is initially in state $|0\rangle$. The first $\pi/2$ MW pulse generates the superposition of the spin states, and the second $\pi/2$ pulse converts one component of the coherence to population, which then can be read out by a laser pulse.
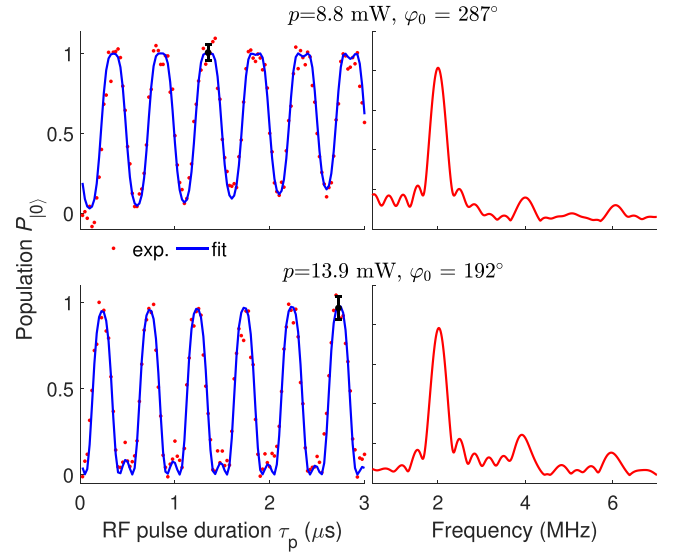

FIG. 2. Experimental results demonstrating the effect of the longitudinal component of the rf field on the electron spin at two different rf powers p of the rf pulses. The left column shows the population $P_{|0\rangle}$ as a function of the rf pulse duration τ_p. The error bars indicate the photon counting statistics. The dots represent the experimental data and the curves the fit to function (3), where the phase $\varphi_z(\tau_p)$ is given by Eq. (9). The right column shows the corresponding absolute value spectra.

longitudinal component of the rf field [46]. It commutes with the static system Hamiltonian and changes the energy levels and transition frequencies in first order. The second term couples to the transverse spin component S_x. It does not generate a first-order shift, but the resulting second-order effect in the rf field amplitude, which is known as the Bloch-Siegert shift (BSS) [47,48], also contributes to a shift of the energy levels. Since the second-order effect also commutes with the static Hamiltonian, it can be treated independently of the effect of the longitudinal term.

We start with the longitudinal term, which shifts the energy levels of the electron spin by $\delta\mathcal{E}_m = -\omega_z m \sin(\omega_{\mathrm{rf}} t + \varphi_0)$, where m is the corresponding eigenvalue of S_z. A coherence between states $|m\rangle$, $|m'\rangle$ then acquires a phase

$$\varphi_z(\tau_p) = -\omega_z(m - m')\int_0^{\tau_p}\sin(\omega_{\mathrm{rf}} t + \varphi_0)dt$$
$$= \alpha[\cos(\omega_{\mathrm{rf}}\tau_p + \varphi_0) - \cos(\varphi_0)], \quad (2)$$

where $\alpha = (m - m')\omega_z/\omega_{\mathrm{rf}}$ and τ_p is the duration of the rf pulse.

The effects of the acquired phase can be observed using the pulse sequence shown in Fig. 1. The initial state of the electron spin is $|m\rangle$. The first $\pi/2$ pulse generates the superposition of states $|m\rangle$ and $|m'\rangle$. The second $\pi/2$ pulse converts part of the coherence to population, which can be read out. The resulting signal depends on φ_z as

$$P_{|0\rangle}(\tau_p) = [1 - \cos\varphi_z(\tau_p)]/2. \quad (3)$$

For spectral analysis, we write $\cos\varphi_z(\tau_p)$ as a Fourier series by using

$$\cos\varphi_z(\tau_p) = \cos(\alpha\cos\varphi_0)S_c + \sin(\alpha\cos\varphi_0)S_s. \quad (4)$$

Here, $S_c \equiv \cos(\alpha\cos x)$, $S_s \equiv \sin(\alpha\cos x)$ are a Fourier series,

$$S_c = J_0(\alpha) + 2\sum_{n=1}^{\infty}(-1)^n J_{2n}(\alpha)\cos(2nx),$$

$$S_s = 2\sum_{n=0}^{\infty}(-1)^n J_{2n+1}(\alpha)\cos[(2n+1)x], \quad (5)$$

where $x = \omega_{\mathrm{rf}}\tau_p + \varphi_0$ and $J_\nu(z)$ is the Bessel function of the first kind [49].

For the discussion of the second-order effect (BSS), we consider a transition between two electron states with transition frequency Ω_0. The BSS shifts this resonance frequency by

$$\omega_{\mathrm{BS}} = \omega_x^2/(2\Omega_0). \quad (6)$$

The acquired phase of the coherence between states $|m\rangle$ and $|m'\rangle$ is

$$\varphi_x(\tau_p) = \omega_{\mathrm{BS}}\tau_p. \quad (7)$$

The effects of the BSS can also be observed using the pulse sequence in Fig. 1. Equation (3) becomes then

$$P_{|0\rangle}(\tau_p) = \{1 - \cos[\varphi_z(\tau_p) + \varphi_x(\tau_p)]\}/2. \quad (8)$$

Experimental demonstration for short signals. We choose the electron states $|m_S = 0\rangle$ and $|m_S = -1\rangle$ for a quantitative study of these effects, starting with the first-order effect. We first initialize the electron into $|m_S = 0\rangle$ with the details given in Sec. I of the Supplemental Material (SM) [50]. According to Eqs. (4) and (5), the first-order effect contributes components at frequencies $n\omega_{\mathrm{rf}}$. On a timescale shorter than the dephasing time of the electron spin ($T_2^* \approx 22$ μs, see Sec. I of the SM [50]), we use the pulse sequence shown in Fig. 1, with the rf frequency $\omega_{\mathrm{rf}}/(2\pi) = 2$ MHz [51]. The details such as the total sequence duration and repetitions of the sequence are listed in SM Sec. VII [50].

Figure 2 shows the experimental results for two different rf powers and initial phases φ_0. The experimental time-domain signals (Fig. 2 left) show the expected periodicity in

TABLE I. Measured field amplitudes. $\omega_z/2\pi$ was obtained from the experimental data in Fig. 2, and $\omega_x/2\pi$ and $\omega_{dc}/2\pi$ from Fig. 5.

	$p = 8.8$	13.9 (mW)
$\omega_z/2\pi$ (MHz)	2.66 ± 0.02	3.24 ± 0.12
$\omega_x/2\pi$ (MHz)	35.2 ± 0.7	44 ± 1
$\omega_{dc}/2\pi$ (MHz)	-0.20 ± 0.01	-0.25 ± 0.01

$2\pi/\omega_{rf} = 0.5$ µs. The frequency of the field can be measured here directly either in the spectrum or by fitting the experimental data, without adjusting the experimental parameter. After several periods, the signal deviates from exact periodicity. These deviations are mostly due to the dc component of the field and to the second-order effect, as discussed below. To include them in the fitting function, we modify $\varphi_z(\tau_p)$ in Eq. (2) to

$$\varphi_f(\tau_p) = \varphi_z(\tau_p) + (\omega_{dc} + \omega_{BS})\tau_p + \delta. \quad (9)$$

Here, ω_{dc} is the projection of the dc component of the applied field to the z axis and ω_{BS} the second-order contribution of the ac component, which generates a time-averaged frequency shift [see Eq. (6) and Refs. [47,48]]. ω_{dc} and ω_{BS} have different dependencies on the rf power level: ω_{dc} increases with the square root of the power and ω_{BS} increases quadratically with ω_x and thus linearly with the power. We can therefore separate the contributions by evaluating them at different power levels; details are given in SM Sec. IV [50]. The constant term δ appears to be due to transients generated by switching the rf pulse on and off with a finite rise time. The values for α, β, and δ obtained by fitting the experimental data are listed in the SM Sec. III A [50]. The field amplitudes ω_z at two different power levels are listed in Table I. The ratio between the two measured values of ω_z is 1.22, consistent with the ratio of the field strengths $\sqrt{13.9/8.8} = 1.26$.

The periodicity of these data suggests an analysis in the frequency domain. As shown in the Fourier transforms of the time-domain data in Fig. 2, peaks appear at integer multiples of the rf frequency $n\omega_{rf}$, in agreement with Eq. (4). Using the spectra in Fig. 2, we obtain the values of $\omega_z/2\pi$ consistent with the results obtained from the time-domain signals. The results are presented in SM Sec. III B [50], together with additional details.

Measurement of the second-order shift. Since second-order shifts are significantly smaller, measuring them requires higher precision and thus longer signals. Figure 3 shows some experimental results obtained with the pulse sequence in Fig. 1 and 8.8 mW rf power. The time-domain signal can be fitted by

$$P_{|0\rangle}(\tau_p) = \{1 - e^{-\tau_p/T_2^*}\cos[\varphi_f(\tau_p)]\}/2, \quad (10)$$

where $T_2^* = 22$ µs, estimated from the free induction decay (FID) measurement (see SM Sec. I [50]).

To reduce noise-induced dephasing during these longer measurement periods, we use DD pulses [18,21]. The pulse sequence shown in Fig. 4 includes two refocusing pulses with a $\pi/2$ phase shift for compensating cumulative pulse errors [52]. More experiment details are present in SM Sec. VII [50]. The phase generated by the rf pulse is not canceled by the DD
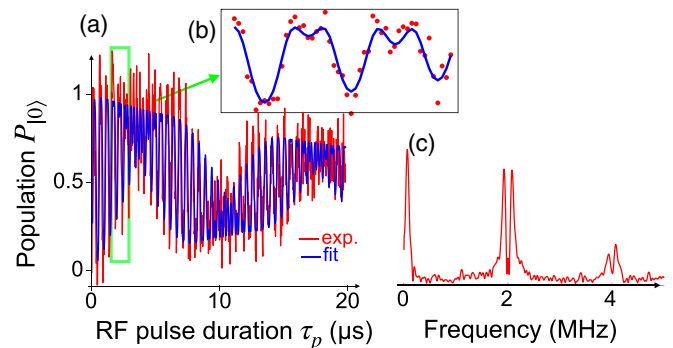

FIG. 3. Experimental results demonstrating first- and second-order contributions to the phase acquired by the electron spins by the pulse sequence shown in Fig. 1. (a) The population $P_{|0\rangle}$ as a function of the rf pulse duration τ_p. The red curve indicate the experiment data and the blue curves the fit by the function in Eq. (10). (b) Details for a short section, where the experimental data are indicated by solid circles. (c) Absolute value spectrum obtained from the experimental data in (a).

pulses, since the rf is applied only between the two refocusing pulses. This approach requires controllable sources, in much the same way as in earlier experiments (e.g., Ref. [23]) but provides high precision compared to the experiment without DD shown in Fig. 3.

The resulting phase is given by Eq. (9) and it is again transferred into a measurable population by the final $\pi/2$ pulse, resulting in the signal

$$P_{|0\rangle}(\tau_p) = \{1 + \cos[\varphi_f(\tau_p)]\}/2. \quad (11)$$

Figure 5 (left-hand side) shows the measured signal $P_{|0\rangle}(\tau_p)$, for two different powers. Compared with the signal in Fig. 3(a), the decay due to the dephasing effect is negligible, since the DD pulses extend the dephasing time up to 1.2 ms [48]. The fast oscillation (period <1 µs) is due to the first-order effect covered above, while the slower oscillation, whose period decreases drastically when the power level increases, is the topic here. The Fourier transforms of the time-domain data shown in Fig. 5 (right-hand side) contain peaks at the frequencies $|n\omega_{rf} \pm (\omega_{dc} + \omega_{BS})|/2\pi$, with $n = 0$, 1, and 2. The values of the measured frequencies are listed in SM Sec. III C [50]. The calculated field amplitudes
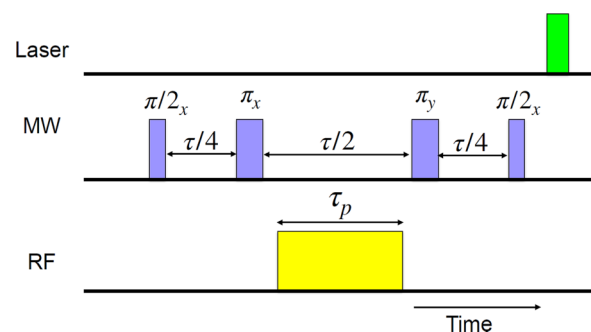

FIG. 4. Pulse sequence for sensing rf fields over longer timescales. The two π pulses are used to extend the coherence time of the electron spin. The other pulses are identical to those in Fig. 1.
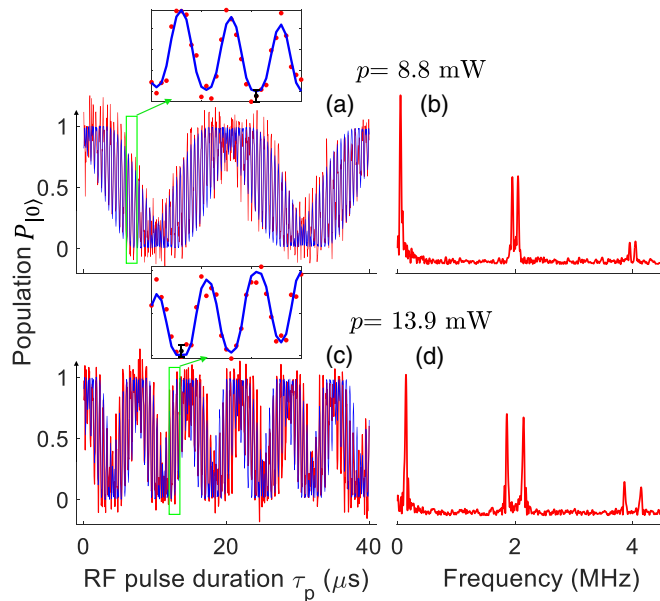
FIG. 5. Experimental results demonstrating first- and second-order contributions to the phase acquired by the electron spins at two different rf powers, using the pulse sequence shown in Fig. 4. The left column shows the population $P_{|0\rangle}$ as a function of the rf pulse duration τ_p. The red curves indicate the experimental data and the blue curves show the fit to function (11). The right column shows the absolute value spectra obtained from the experimental data on the left.

ω_{dc} and ω_x are listed in Table I, where Eq. (6) is used and Ω_0 is measured as 2.475 151 GHz. These values agree with those obtained with the simpler pulse sequence in Fig. 1 (for details, see SM Sec. IV [50]), but provide higher precision and accuracy. From the measured components ω_z and ω_x, we can estimate the angle θ between the NV axis and the rf field as $\theta \approx 86°$.

Discussion and conclusion. This Letter introduces a protocol for measuring time-dependent magnetic fields covering a large frequency range, starting at zero, in contrast to previous works that focused on dc fields or ac fields within a very narrow frequency range. The experimental implementation is performed using the electron spin of an NV center in diamond, offering the ultimate spatial resolution, compared with the schemes based on ensembles [37,38,42]. It can detect components parallel as well as perpendicular to the quantization axis. The field sensitivity of this broadband technique is lower than for narrowband approaches and depends on the direction of the fields with respect to the symmetry axis of the center. The parallel (secular) component scales linearly with the amplitude of the field and inversely with its frequency. For the experimentally tested case of $\omega_{rf}/(2\pi) = 2$ MHz, we found a field sensitivity of 3.7 µT. For the transverse component, the signal scales with the square root of the field amplitude but does not depend on the rf frequency. The resulting sensitivity is proportional to the square root of the resonance linewidth. In the experiment with dynamical decoupling, the field sensitivity is 5.8 µT. Details are given in SM Sec. VI [50]. Compared to methods based on spin locking [35], our method covers a much larger frequency range. Unlike the previous work [23], where only the field components aligned with the symmetry axis of the NV center were considered and the effect of perpendicular components was assumed to be negligible, we consider fields with arbitrary orientation and show how the orientation with respect to the symmetry axis can be extracted from the measured data. This is helpful, e.g., in the case of quantum computing using hybrid quantum registers where rf fields used to control the nuclear spins have unwanted side effects on the electron spin [46]. The secular component of this effect can be eliminated by orienting the rf field perpendicular to the symmetry axis of the NV center.

In the present work, we used a single NV center as the sensor and showed how it can be used to access different components of a magnetic field. The approach can easily be extended to multiple centers and ensembles [37,38,53–55]. Using centers with different orientations would allow, e.g., to improve the accuracy and precision of the amplitude and all the orientational information on the field.

[1] C. L. Degen, F. Reinhard, and P. Cappellaro, Quantum sensing, Rev. Mod. Phys. **89**, 035002 (2017).

[2] N. De Zanche, C. Barmet, J. A. Nordmeyer-Massner, and K. P. Pruessmann, NMR probes for measuring magnetic fields and field dynamics in MR systems, Magn. Reson. Med. **60**, 176 (2008).

[3] J. Kitching, S. Knappe, and E. A. Donley, Atomic sensors – a review, IEEE Sens. J. **11**, 1749 (2011).

[4] M. Jiang, W. Xu, Q. Li, Z. Wu, D. Suter, and X. Peng, Interference in atomic magnetometry, Adv. Quantum Technol. **3**, 2000078 (2020).

[5] M. Brownnutt, M. Kumph, P. Rabl, and R. Blatt, Ion-trap measurements of electric-field noise near surfaces, Rev. Mod. Phys. **87**, 1419 (2015).

[6] K. A. Gilmore, M. Affolter, R. J. Lewis-Swan, D. Barberena, E. Jordan, A. M. Rey, and J. J. Bollinger, Quantum-enhanced sensing of displacements and electric fields with two-dimensional trapped-ion crystals, Science **373**, 673 (2021).

[7] H. Fan, S. Kumar, J. Sedlacek, H. Kuebler, S. Karimkashi, and J. P. Shaffer, Atom based rf electric field sensing, J. Phys. B: At., Mol. Opt. Phys. **48**, 202001 (2015).

[8] R. C. Jaklevic, J. Lambe, J. E. Mercereau, and A. H. Silver, Macroscopic quantum interference in superconductors, Phys. Rev. **140**, A1628 (1965).

[9] M. Hatridge, R. Vijay, D. H. Slichter, J. Clarke, and I. Siddiqi, Dispersive magnetometry with a quantum limited SQUID parametric amplifier, Phys. Rev. B **83**, 134501 (2011).

[10] R. L. Fagaly, Superconducting quantum interference device instruments and applications, Rev. Sci. Instrum. **77**, 101101 (2006).

[11] L. Rondin, J.-P. Tetienne, T. Hingant, J.-F. Roch, P. Maletinsky, and V. Jacques, Magnetometry with nitrogen-vacancy defects in diamond, Rep. Prog. Phys. **77**, 056503 (2014).

[12] J. F. Barry, J. M. Schloss, E. Bauch, M. J. Turner, C. A. Hart, L. M. Pham, and R. L. Walsworth, Sensitivity optimization for NV-diamond magnetometry, Rev. Mod. Phys. **92**, 015004 (2020).

[13] D. Suter and F. Jelezko, Single-spin magnetic resonance in the nitrogen-vacancy center of diamond, Prog. Nucl. Magn. Reson. Spectrosc. **98-99**, 50 (2017).

[14] R. Schirhagl, K. Chang, M. Loretz, and C. L. Degen, Nitrogen-vacancy centers in diamond: nanoscale sensors for physics and biology, Annu. Rev. Phys. Chem. **65**, 83 (2014).

[15] M. A. Nielsen and I. L. Chuang, *Quantum Computation and Quantum Information* (Cambridge University Press, Cambridge, UK, 2000).

[16] J. Stolze and D. Suter, *Quantum Computing: A Short Course from Theory to Experiment*, 2nd ed. (Wiley-VCH, Berlin, 2008).

[17] A. Zwick, D. Suter, G. Kurizki, and G. A. Alvarez, Precision limits of tissue microstructure characterization by magnetic resonance imaging, Phys. Rev. Appl. **14**, 024088 (2020).

[18] D. Suter and G. A. Alvarez, Protecting quantum information against environmental noise, Rev. Mod. Phys. **88**, 041001 (2016).

[19] G. A. Alvarez and D. Suter, Measuring the spectrum of colored noise by dynamical decoupling, Phys. Rev. Lett. **107**, 230501 (2011).

[20] A. M. Souza, G. A. Alvarez, and D. Suter, Robust dynamical decoupling for quantum computing and quantum memory, Phys. Rev. Lett. **106**, 240501 (2011).

[21] A. M. Souza, G. A. Alvarez, and D. Suter, Robust dynamical decoupling, Phil. Trans. R. Soc. A **370**, 4748 (2012).

[22] J. M. Taylor, P. Cappellaro, L. Childress, L. Jiang, D. Budker, P. R. Hemmer, A. Yacoby, R. Walsworth, and M. D. Lukin, High-sensitivity diamond magnetometer with nanoscale resolution, Nat. Phys. **4**, 810 (2008).

[23] G. Balasubramanian, P. Neumann, D. Twitchen, M. Markham, R. Kolesov, N. Mizuochi, J. Isoya, J. Achard, J. Beck, J. Tissler *et al.*, Ultralong spin coherence time in isotopically engineered diamond, Nat. Mater. **8**, 383 (2009).

[24] V. K. Kavatamane, D. Duan, S. R. Arumugam, N. Raatz, S. Pezzagna, J. Meijer, and G. Balasubramanian, Probing phase transitions in a soft matter system using a single spin quantum sensor, New J. Phys. **21**, 103036 (2019).

[25] T. Unden, P. Balasubramanian, D. Louzon, Y. Vinkler, M. B. Plenio, M. Markham, D. Twitchen, A. Stacey, I. Lovchinsky, A. O. Sushkov *et al.*, Quantum metrology enhanced by repetitive quantum error correction, Phys. Rev. Lett. **116**, 230502 (2016).

[26] J. Zhang, R. Laflamme, and D. Suter, Experimental implementation of encoded logical qubit operations in a perfect quantum error correcting code, Phys. Rev. Lett. **109**, 100503 (2012).

[27] S. Zaiser, T. Rendler, I. Jakobi, T. Wolf, S.-Y. Lee, S. Wagner, V. Bergholm, T. Schulte-Herbrueggen, P. Neumann, and J. Wrachtrup, Enhancing quantum sensing sensitivity by a quantum memory, Nat. Commun. **7**, 12279 (2016).

[28] X. Peng, D. Suter, and D. A. Lidar, High fidelity quantum memory via dynamical decoupling: theory and experiment, J. Phys. B: At., Mol. Opt. Phys. **44**, 154003 (2011).

[29] J. H. Shim, I. Niemeyer, J. Zhang, and D. Suter, Room-temperature high-speed nuclear-spin quantum memory in diamond, Phys. Rev. A **87**, 012301 (2013).

[30] M. Lovric, P. Glasenapp, D. Suter, B. Tumino, A. Ferrier, P. Goldner, M. Sabooni, L. Rippe, and S. Kröll, Hyperfine characterization and spin coherence lifetime extension in $Pr^{3+}:La_2(WO_4)_3$, Phys. Rev. B **84**, 104417 (2011).

[31] M. Lovric, D. Suter, A. Ferrier, and P. Goldner, Faithful solid state optical memory with dynamically decoupled spin wave storage, Phys. Rev. Lett. **111**, 020503 (2013).

[32] L. Childress, M. V. Gurudev Dutt, J. M. Taylor, A. S. Zibrov, F. Jelezko, J. Wrachtrup, P. R. Hemmer, and M. D. Lukin, coherent dynamics of coupled electron and nuclear spin qubits in diamond, Science **314**, 281 (2006).

[33] M. H. Abobeih, J. Randall, C. E. Bradley, H. P. Bartling, M. A. Bakker, M. J. Degen, M. Markham, D. J. Twitchen, and T. H. Taminiau, Atomic-scale imaging of a 27-nuclear-spin cluster using a quantum sensor, Nature (London) **576**, 411 (2019).

[34] Y. Wu, F. Jelezko, M. B. Plenio, and T. Weil, Diamond quantum devices in biology, Angew. Chem., Int. Ed. **55**, 6586 (2016).

[35] M. Loretz, T. Rosskopf, and C. L. Degen, Radio-frequency magnetometry using a single electron spin, Phys. Rev. Lett. **110**, 017602 (2013).

[36] G. Wang, Y.-X. Liu, Y. Zhu, and P. Cappellaro, Nanoscale vector ac magnetometry with a single nitrogen-vacancy center in diamond, Nano Lett. **21**, 5143 (2021).

[37] P. Wang, Z. Yuan, P. Huang, X. Rong, M. Wang, X. Xu, C. Duan, C. Ju, F. Shi, and J. Du, High-resolution vector microwave magnetometry based on solid-state spins in diamond, Nat. Commun. **6**, 6631 (2015).

[38] J. M. Schloss, J. F. Barry, M. J. Turner, and R. L. Walsworth, Simultaneous broadband vector magnetometry using solid-state spins, Phys. Rev. Appl. **10**, 034044 (2018).

[39] Y.-X. Liu, A. Ajoy, and P. Cappellaro, Nanoscale vector dc magnetometry via ancilla-assisted frequency up-conversion, Phys. Rev. Lett. **122**, 100501 (2019).

[40] X.-D. Chen, F.-W. Sun, C.-L. Zou, J.-M. Cui, L.- M. Zhou, and G.-C. Guo, Vector magnetic field sensing by a single nitrogen vacancy center in diamond, Europhys. Lett. **101**, 67003 (2013).

[41] G. Balasubramanian, I. Chan, R. Kolesov, M. Al-Hmoud, J. Tisler, C. Shin, C. Kim, A. Wojcik, P. R. Hemmer, A. Krueger *et al.*, Nanoscale imaging magnetometry with diamond spins under ambient conditions, Nature (London) **455**, 648 (2008).

[42] Z. Wang, F. Kong, P. Zhao, Z. Huang, P. Yu, Y. Wang, F. Shi, and J. Du, Picotesla magnetometry of microwave fields with diamond sensors, Sci. Adv. **8**, eabq8158 (2022).

[43] T. Teraji, T. Taniguchi, S. Koizumi, Y. Koide, and J. Isoya, Effective use of source gas for diamond growth with isotopic enrichment, Appl. Phys. Express **6**, 055601 (2013).

[44] J. Zhang, J. H. Shim, I. Niemeyer, T. Taniguchi, T. Teraji, H. Abe, S. Onoda, T. Yamamoto, T. Ohshima, J. Isoya *et al.*, Experimental implementation of assisted quantum adiabatic passage in a single spin, Phys. Rev. Lett. **110**, 240501 (2013).

[45] K. D. Jahnke, B. Naydenov, T. Teraji, S. Koizumi, T. Umeda, J. Isoya, and F. Jelezko, Long coherence time of spin qubits in ^{12}C enriched polycrystalline chemical vapor deposition diamond, Appl. Phys. Lett. **101**, 012405 (2012).

[46] M. Hirose and P. Cappellaro, Coherent feedback control of a single qubit in diamond, Nature (London) **532**, 77 (2016).

[47] F. Bloch and A. Siegert, Magnetic resonance for nonrotating fields, Phys. Rev. **57**, 522 (1940).

[48] J. Zhang, S. Saha, and D. Suter, Bloch-Siegert shift in a hybrid quantum register: quantification and compensation, Phys. Rev. A **98**, 052354 (2018).

[49] A. P. Saiko, S. A. Markevich, and R. Fedaruk, Possibility of direct observation of the Bloch-Siegert shift in coherent dynamics of multiphoton Raman transitions, JETP Lett. **110**, 441 (2019).

[50] See Supplemental Material at http://link.aps.org/supplemental/10.1103/PhysRevResearch.5.L022026 for details of the preparation of initial state, rf pulses, additional data, separation of ω_{dc} and ω_{BS}, and analysis on field sensitivity.

[51] The specific frequency was chosen to be sufficiently far from the resonance frequency of the NMR transitions, in order to avoid effects that are not related to the sensing via the electron spin.

[52] T. Gullion, D. B. Baker, and M. S. Conradi, New, compensated Carr-Purcell sequences, J. Magn. Reson. (1969-1992) **89**, 479 (1990).

[53] T. Fukui, Y. Doi, T. Miyazaki, Y. Miyamoto, H. Kato, T. Matsumoto, T. Makino, S. Yamasaki, R. Morimoto, and N. Tokuda, Perfect selective alignment of nitrogen-vacancy centers in diamond, Appl. Phys. Express **7**, 055201 (2014).

[54] J. Michl, T. Teraji, S. Zaiser, I. Jakobi, G. Waldherr, F. Dolde, P. Neumann, M. W. Doherty, N. B. Manson, J. Isoya, and J. Wrachtrup, Perfect alignment and preferential orientation of nitrogen-vacancy centers during chemical vapor deposition diamond growth on (111) surfaces, Appl. Phys. Lett. **104**, 102407 (2014).

[55] M. Lesik, J.-P. Tetienne, A. Tallaire, J. Achard, V. Mille, A. Gicquel, J.-F. Roch, and V. Jacques, Perfect preferential orientation of nitrogen-vacancy defects in a synthetic diamond sample, Appl. Phys. Lett. **104**, 113107 (2014).